Self-assembly of magnetite nanocubes into helical superstructures

Gurvinder Singh *et al.*

Science **345**, 1149 (2014);
DOI: 10.1126/science.1254132

5. Y. Nambu, *Phys. Rev. Lett.* **4**, 380–382 (1960).
6. C. M. Varma, *J. Low Temp. Phys.* **126**, 901–909 (2002).
7. G. E. Volovik, M. A. Zubkov, *J. Low Temp. Phys.* **175**, 486–497 (2014).
8. P. W. Anderson, *Phys. Rev.* **130**, 439–442 (1963).
9. P. W. Higgs, *Phys. Lett.* **12**, 132–133 (1964).
10. A. F. Volkov, S. M. Kogan, *Zh. Eksp. Teor. Fiz.* **65**, 2038 (1973) [*Sov. Phys. JETP* **38**, 1018 (1974)].
11. R. A. Barankov, L. S. Levitov, B. Z. Spivak, *Phys. Rev. Lett.* **93**, 160401 (2004).
12. E. A. Yuzbashyan, M. Dzero, *Phys. Rev. Lett.* **96**, 230404 (2006).
13. T. Papenkort, V. M. Axt, T. Kuhn, *Phys. Rev. B* **76**, 224522 (2007).
14. N. Tsuji, M. Eckstein, P. Werner, *Phys. Rev. Lett.* **110**, 136404 (2013).
15. Y. Barlas, C. M. Varma, *Phys. Rev. B* **87**, 054503 (2013).
16. R. Matsunaga *et al.*, *Phys. Rev. Lett.* **111**, 057002 (2013).
17. R. Sooryakumar, M. V. Klein, *Phys. Rev. Lett.* **45**, 660–662 (1980).
18. P. B. Littlewood, C. M. Varma, *Phys. Rev. Lett.* **47**, 811–814 (1981).
19. J. Hebling, K.-L. Yeh, M. C. Hoffmann, B. Bartal, K. A. Nelson, *J. Opt. Soc. Am. B* **25**, B6 (2008).
20. For a review, see, e.g., T. Kampfrath, K. Tanaka, K. A. Nelson, *Nat. Photonics* **7**, 680–690 (2013).
21. F. Junginger *et al.*, *Phys. Rev. Lett.* **109**, 147403 (2012).
22. R. Matsunaga, R. Shimano, *Phys. Rev. Lett.* **109**, 187002 (2012).
23. R. Shimano, S. Watanabe, R. Matsunaga, *J. Infrared. Milli. Terahz. Waves* **33**, 861–869 (2012).
24. K. Makise, H. Terai, M. Takeda, Y. Uzawa, Z. Wang, *IEEE Trans. Appl. Supercond.* **21**, 139–142 (2011).
25. Supplementary materials are available on *Science* Online.
26. P. W. Anderson, *Phys. Rev.* **112**, 1900–1916 (1958).
27. Recently, a time-resolved Raman experiment in a high-T_c cuprate has been reported and accounted for by the dynamics of individual pseudospins corresponding to the charge fluctuations induced by an impulsive stimulated Raman process (*38*).
28. N. Tsuji, H. Aoki, http://arxiv.org/abs/1404.2711.
29. The conversion efficiency was estimated without compensating the frequency dependence of the EO-sampling detection coefficient for the 1-mm-thick ZnTe crystal. The correction would make the conversion efficiency even higher.
30. A. Kawakami, Y. Uzawa, Z. Wang, *Physica C* **412–414**, 1455–1458 (2004).
31. P. V. Carlson, A. M. Goldman, *Phys. Rev. Lett.* **34**, 11–15 (1975).
32. Such a study may reveal the underlying coupling strength of the superconducting order parameter with other excitations; for the case of charge-density-wave system; see, e.g., (*37*).
33. L. P. Gorkov, G. M. Eliashberg, *Zh. Eksp. Teor. Fiz.* **54**, 612 (1968) [*Sov. Phys. JETP* **27**, 328 (1968)].
34. J. C. Amato, W. L. McLean, *Phys. Rev. Lett.* **37**, 930–933 (1976).
35. O. Entin-Wohlman, *Phys. Rev. B* **18**, 4762–4767 (1978).
36. W. Zimmermann, E. H. Brandt, M. Bauer, E. Seider, L. Genzel, *Physica C* **183**, 99–104 (1991).
37. H. Schaefer, V. V. Kabanov, J. Demsar, *Phys. Rev. B* **89**, 045106 (2014).
38. B. Mansart *et al.*, *Proc. Natl. Acad. Sci. U.S.A.* **110**, 4539 (2013).

ACKNOWLEDGMENTS

This work was supported by a Grant-in-Aid for Scientific Research (grant nos. 25800175, 22244036, 20110005, 25104709, 25800192, and 26247057) and Advanced Photon Science Alliance by the Photon Frontier Network Program from Ministry of Education, Culture, Sports, Science, and Technology.

SUPPLEMENTARY MATERIALS

www.sciencemag.org/content/345/6201/1145/suppl/DC1
Materials and Methods
Supplementary Text
Figs. S1 to S3
References

11 April 2014; accepted 24 June 2014
Published online 10 July 2014;
10.1126/science.1254697

NANOMATERIALS

Self-assembly of magnetite nanocubes into helical superstructures

Gurvinder Singh,[1] Henry Chan,[2] Artem Baskin,[2] Elijah Gelman,[1] Nikita Repnin,[2] Petr Král,[2,3]* Rafal Klajn[1]*

Organizing inorganic nanocrystals into complex architectures is challenging and typically relies on preexisting templates, such as properly folded DNA or polypeptide chains. We found that under carefully controlled conditions, cubic nanocrystals of magnetite self-assemble into arrays of helical superstructures in a template-free manner with >99% yield. Computer simulations revealed that the formation of helices is determined by the interplay of van der Waals and magnetic dipole-dipole interactions, Zeeman coupling, and entropic forces and can be attributed to spontaneous formation of chiral nanocube clusters. Neighboring helices within their densely packed ensembles tended to adopt the same handedness in order to maximize packing, thus revealing a novel mechanism of symmetry breaking and chirality amplification.

Nanoscale particles often self-assemble into superstructures with distinctive spatial arrangements that are difficult to predict based on the nature of their building blocks (*1*–*9*). This is because the stabilization of such self-assembled materials results from a delicate competition among forces of comparable magnitudes, originating in van der Waals, Coulombic, magnetic, and other types of particle interactions (*10*). Although the structures of some systems are dominated by forces of a common origin [such as electrostatic interactions that govern the formation of open-lattice assemblies of peptide filaments (*7*) or colloidal crystals with a diamond-like lattice (*3*)], it is typically the interplay between various nanoscale forces that leads to the formation of highly complex materials, such as nanocrystal superlattices exhibiting polymorphism (*11*, *12*).

Self-assembly of nanoparticles driven by competing forces can result in truly unique structures, the diversity and complexity of which could be particularly striking if the building blocks were simultaneously coupled by short- and long-range forces of different symmetries. Such frustration could arise in ensembles of magnetic nanocrystals (NCs) whose axes of preferential magnetization (so-called "easy" axes) do not correspond to any of the directions favoring close packing. In the case of magnetite—the most abundant magnetic material on Earth, also present inside multiple living organisms in the form of NCs (*13*)—this condition is best fulfilled by cubic-shaped particles, whose easy axes (the [111] crystallographic direction; see Fig. 1B) connect two diagonally opposite corners of each cube. However, complex superstructures resulting from the competition between the shape anisotropy (favoring face-to-face interactions) and the magnetocrystalline anisotropy (favoring corner-to-corner interactions) have not been reported, perhaps because the former type of anisotropy typically dominates the latter (*14*, *15*). Here, we investigated the self-assembly of magnetite NCs at the liquid-air interface in the presence of external magnetic fields. Depending on the density of the NCs, we identified different types of self-assembled superstructures, including one-dimensional belts as well as single, double, and triple helices.

In our experimental setup (Fig. 1A), a drop of hexane solution of relatively monodisperse magnetite nanocubes (*16*–*18*) [average edge length = 13.4 nm, corner bluntness ρ = 23%; Fig. 1B and figs. S1, S2, S3, and S28A (*19*)] containing excess oleic acid (OA) was placed at the diethylene glycol (DEG)–air interface (*20*, *21*) in the presence of a magnetizing field (whose strength H was regulated in the range of 0 to 700 G). The solvent was allowed to evaporate within ~10 min. Our NCs are in the superparamagnetic (SPM) size regime; that is, the collective dipoles of individual NCs thermally fluctuate, and the directions of the dipole moments are random. When the NCs were exposed to an external magnetic field, the collective dipoles became partially aligned with the field direction, which allowed for the cooperative magnetic dipole-dipole coupling between the NCs. The resulting chains of single particles (fig. S9) further aggregated as the solvent evaporated, ultimately giving rise to higher-order superstructures at the solvent-air interface. These superstructures could be transferred onto a substrate of choice (e.g., a carbon-coated copper grid or a silicon wafer for inspection) (Fig. 1A). On the basis of electron microscopy images, we estimate that fewer than 1% of the NCs remained unassembled.

[1]Department of Organic Chemistry, Weizmann Institute of Science, Rehovot 76100, Israel. [2]Department of Chemistry, University of Illinois, Chicago, IL 60607, USA. [3]Department of Physics, University of Illinois, Chicago, IL 60607, USA.
*Corresponding author. E-mail: rafal.klajn@weizmann.ac.il (R.K.); pkral@uic.edu (P.K.)

The nature of these superstructures strongly depended on the surface concentration of the particles (*22*). For concentrations corresponding to less than ~20% of the monolayer coverage (or $\chi < 0.2$, where $\chi = 1$ corresponds to a densely packed monolayer of nanocubes coated with interpenetrating monolayers of OA), no long-range or well-defined structures were found (fig. S10). When $\chi \approx 0.2$, however, NCs assembled into parallel arrays of one-dimensional (1D) belts (*23*, *24*) with high aspect ratios (two to three NCs across and as long as 100 μm; Fig. 1C) and oriented parallel to the applied field (figs. S12 and S13). Individual cubes within these belts had their [100] crystallographic axes oriented parallel to the long axes of the belts (Fig. 1C, inset); thus, we refer to these assemblies as belts$_{100}$. This arrangement of the building blocks maximized the cube-cube contact within the assemblies (i.e., the assemblies were dominated by the shape anisotropy of the particles). The widths of these belts grew with increasing χ and decreasing H values.

To better understand these results, we modeled the arrangements of magnetic dipoles of individual SPM particles within belts by Monte Carlo simulations (*25*) [for additional details on the theoretical model, see (*19*) and figs. S20 to S28]. As Fig. 1D shows, dipole orientations in individual NCs are determined by the competition between dipole-dipole interactions [attractive when two parallel dipoles are within a cone with a polar angle $\theta < \cos^{-1}(1/\sqrt{3}) \approx 54^{\circ}$] and coupling to an external field (Zeeman coupling, which tends to orient the dipoles along the field lines). In the presence of a relatively weak (e.g., 167 G) field, the dipoles assume a "zigzag" configuration "unlocked" from the external field, favoring the magnetocrystalline anisotropy. As the field strength increases, the dipoles become more aligned; eventually, all of them are oriented along the field lines (e.g., at 668 G; Fig. 1D, bottom). However, this dipole arrangement is not favorable because of the magnetic repulsion between cubes lying side by side. To reduce these repulsive interactions, the belts become gradually thinner with increasing applied field [this also explains the equal spacings between individual belts—see, for example, fig. S8C].

In all experiments, the belts' long axes followed the lines of the applied magnetic field. Thus, we could induce the growth of belts tilted with respect to the liquid-air interface by modifying the direction of the applied magnetic field. In the presence of a field directed perpendicular to the liquid-air interface, the NCs assembled into arrays of pillars (fig. S11). Similar to the belts parallel to the interface, individual pillars repelled one another in the presence of a magnetic field, which resulted in their hexagonal close packing (fig. S11D).

Next, we simulated dipole orientations as a function of belt thickness in the presence of a constant applied magnetic field (Fig. 1E; here, H = 167 G). As belts became wider, magnetic dipoles were increasingly decoupled from the external field because of large induced fields

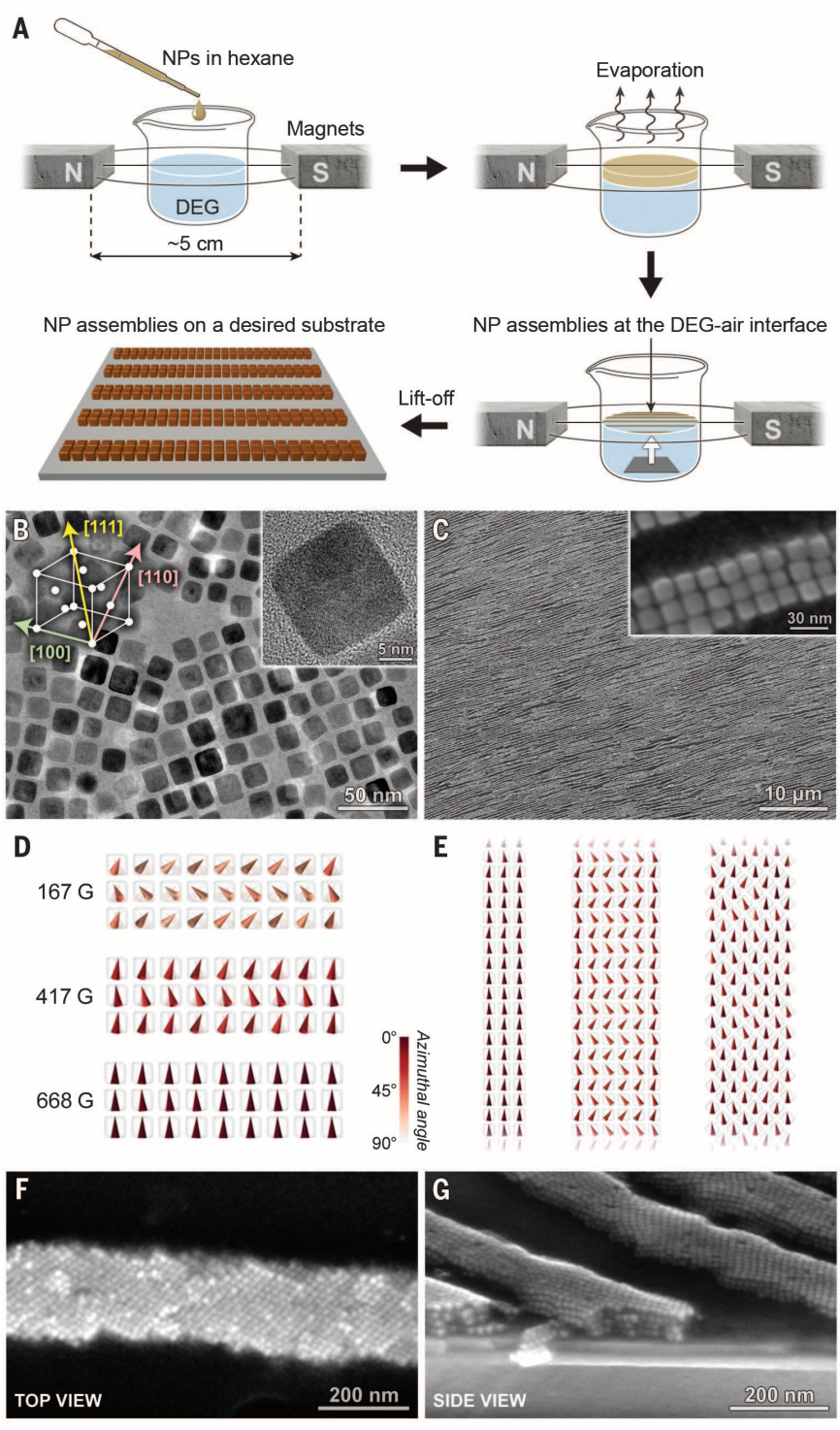

Fig. 1. Self-assembly of one-dimensional nanocube belts. (**A**) Schematic representation of the experimental setup. (**B**) Low- and high-magnification transmission electron microscopy (TEM) images of the building blocks, ~13-nm Fe_3O_4 nanocubes. The [111], [110], and [100] crystallographic directions correspond to the easy, intermediate, and hard axes of magnetization, respectively. (**C**) Low- and high-magnification scanning electron microscopy (SEM) images of belts$_{100}$. (**D**) Averaged orientations of dipoles in a nine-cube-wide belt$_{100}$ in the presence of increasing magnetic fields. (**E**) Orientations of dipoles in belts$_{100}$ of different widths and in a belt$_{110}$ under a relatively weak external field (H = 167 G). The energies of these structures are discussed in (*19*). (**F** and **G**) Top and side views of belts$_{110}$ by SEM.

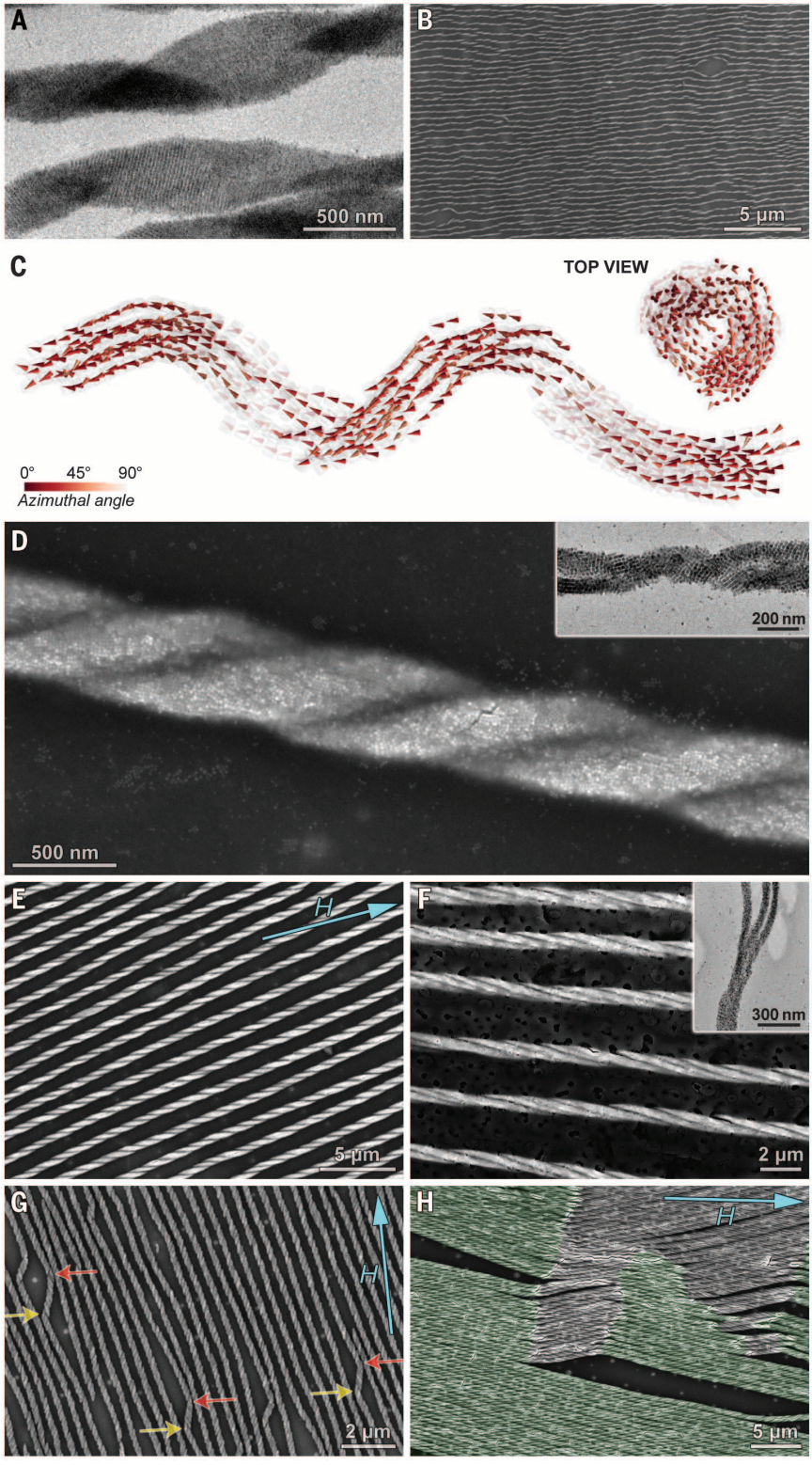

Fig. 2. Self-assembly of helical nanocrystal superstructures. (**A**) TEM image of individual single-stranded helices. (**B**) SEM image of a large array of single-stranded helices. (**C**) Snapshots from Monte Carlo simulations of a one-dimensional belt folding into a helix. (**D**) SEM image of a well-defined double helix. Inset shows a TEM image of two belts wrapping around each another. (**E**) SEM image of an array of double helices. (**F**) An array of triple helices and (inset) the end of a triple helix. (**G**) SEM image showing self-healing of double helices ("chirality self-correction"). Yellow and red arrows indicate sites of chirality inversion. (**H**) Collective switching of chirality. Gray and green colors indicate patches of right- and left-handed helices, respectively. In (E), (G), and (H), blue arrows show the direction of the applied magnetic field.

(Fig. 1E, center). To compensate for the ineffective Zeeman coupling, we rotated each cube by 45° such that their [110] axes were parallel to the field direction; we call the resulting assemblies belts$_{110}$. Although this new arrangement (Fig. 1E, right) was less favorable from the van der Waals interaction point of view (the belts' sides are ridged and not smooth), magnetization along the [110] direction (the "intermediate" axis) occurred more easily than along the [100] ("hard") axis (*26*, *27*) (for quantitative analysis of belts$_{100}$ versus belts$_{110}$, see fig. S22). The formation of belts$_{110}$ was experimentally observed in the narrow range of $1 < \chi < 1.5$ (e.g., Fig. 1, F and G, and fig. S8F).

The most striking manifestation of this trend was observed in experiments performed at $\chi > \sim 1.5$, where the nanocubes tended to orient their [111] axes—that is, the "easy" axes of magnetization—along the magnetic field lines. Because of this arrangement, the belts spontaneously folded (*28*–*30*), giving rise to single-stranded helices (*31*) (Fig. 2A and fig. S14). Monte Carlo simulations confirmed that the formation of helices is accompanied by a free energy minimization (Fig. 2C; see also fig. S23). A detailed analysis revealed that the helices originate from the packing of (transiently) chiral nanocube nuclei, which resulted from the competition of magnetic and spatial symmetries (fig. S21). Similar to the belts discussed above, the helices were evenly spaced and spanned long distances of up to several hundred micrometers (see, for example, Fig. 2B). The properties of these helices were mostly governed by the surface concentration of the NCs: High values of χ entailed large effective magnetic fields, thus promoting a rearrangement of the NCs from the original belt$_{100}$ ensemble (i.e., gradually decreasing the helical pitch). At the same time, high χ values contributed to the widening of the helices (i.e., decreasing interfilament distances). We also observed that individual single-stranded helices tended to wrap around each other to form double-stranded (Fig. 2, D and E, and figs. S15 and S16) or even triple-stranded (Fig. 2F) helices.

The relatively thin helices prepared at $1.5 < \chi < 2.0$ comprised equal populations of intermixed left- and right-handed structures, all oriented parallel to the applied field; Fig. 2A shows a right-handed helix (top) neighboring a left-handed one (bottom). At higher ($\chi > 2.0$) coverages, however, long axes of the helices were tilted with respect to the external field, with the tilt angles θ increasing with increasing χ values. At the same time, we observed that the helices were mostly of the same handedness (e.g., Fig. 2E). A clue to the origin of this selectivity is provided by experiments that yielded ill-defined mixtures of right- and left-handed helices (e.g., Fig. 2, G and H); these two types of helices were tilted at $+\theta$ and $-\theta$ angles with respect to the external magnetic field. To maximize packing within a given area, all of the NC assemblies should be oriented in the same direction and have the same handedness. There was no intrinsic preference for helices of either handedness; each experiment began with the nucleation of either right- or left-handed helices with equal probabilities. As the assembly

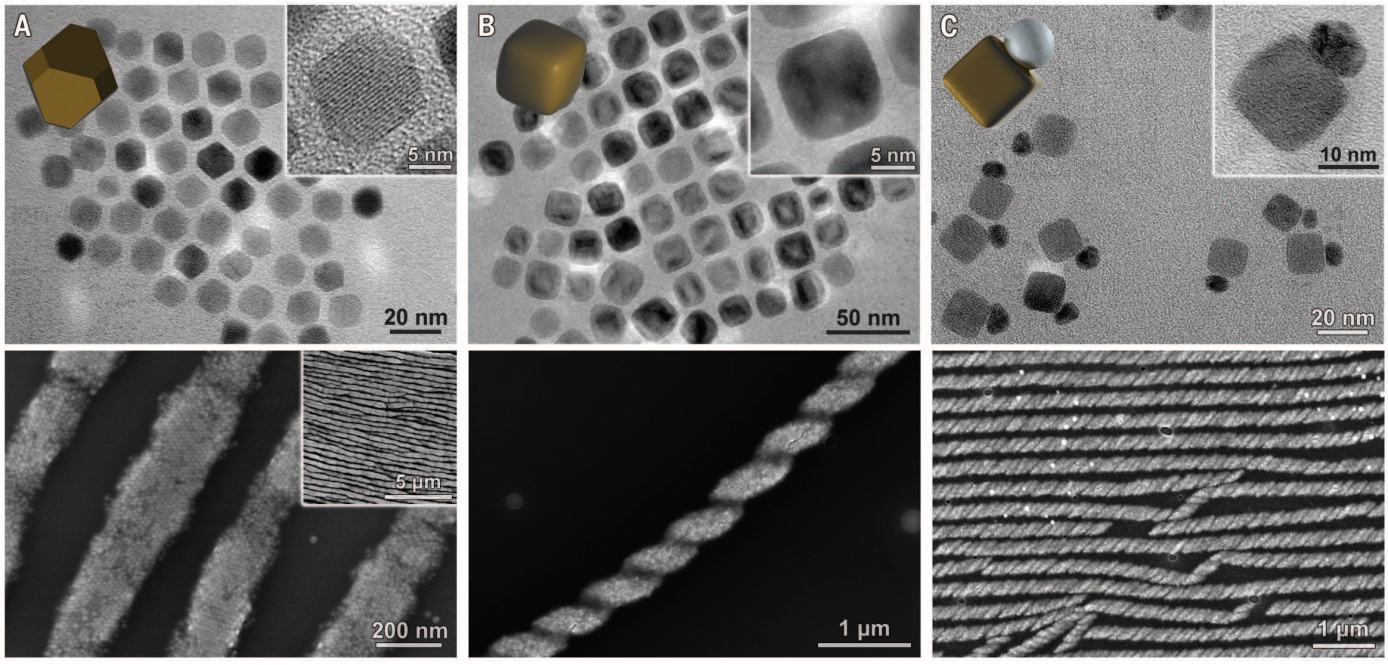

Fig. 3. Self-assembly of Fe_3O_4 nanocrystals of different shapes. (**A**) TEM images of truncated octahedra (top) and an SEM image of 1D belts that they assemble into (bottom; SEM image in the inset shows belts obtained at $\chi = 5$). (**B**) TEM images of rounded cubes (top) and an SEM image of the resulting helix (bottom). (**C**) TEM images of Fe_3O_4-Ag heterodimeric NCs (top) and an SEM image of an ensemble of helices (bottom). Insets in the top row are TEM images of individual nanocrystals obtained at high magnification.

progressed from one side of the dish to the other, however, the chirality of preformed helices determined those of their neighbors, and this process continued to yield large (up to 1 mm^2) domains of "enantiopure" helices.

However, defects were occasionally observed. The red arrows in the ensemble of right-handed helices in Fig. 2G point to sites where chirality inversion took place, giving rise to segments of left-handed structures. Segments of the "wrong" chirality were relatively short; the tendency to maximize packing provided the helices with the ability to "correct" their chirality, as denoted by the yellow arrows in Fig. 2G. We also observed "collective switching of chirality": When a critical number of helices changed their handedness, a domain of inverted helices was stably propagated (Fig. 2H).

To verify the key importance of magnetocrystalline anisotropy for forming helical assemblies, we performed additional assembly experiments using differently shaped magnetite NCs, including spheres, truncated octahedra, and rounded cubes, as well as Fe_3O_4-Ag heterodimeric particles (Fig. 3 and figs. S4 to S7), all of which were in the same size regime (10 to 15 nm). With spherical and octahedral building blocks, we did not observe assemblies other than the 1D belts—even at χ values as high as 5 (Fig. 3A, lower panel, inset). These observations can be rationalized by the lack of competition between the magnetic interactions and close packing: In the case of octahedral NCs, the magnetocrystalline and shape anisotropy act cooperatively to align the particles with their [111] axes oriented parallel to the applied field, whereas the spheres possess no shape anisotropy.

To further clarify these observations, we investigated how cube corner bluntness affected the structure of the assemblies by preparing rounded cubes (Fig. 3B; $\rho = 30\%$). We grew the NCs in the presence of a mixture of surfactants that stabilized the spherical and the cubic morphologies (OA and sodium oleate, respectively). The superstructures obtained at high χ values exhibited helicity, although the helicity was not as prominent as in superstructures obtained from the original cubes; such a result is consistent with the building blocks having shapes intermediate between those of the spheres and the cubes. Finally, we synthesized heterodimers, each comprising a cubic Fe_3O_4 domain and a spherical Ag domain (Fig. 3C, top). The presence of the Ag particles hindered efficient dipole-dipole interactions between the magnetite domain; nonetheless, well-defined helices were observed (Fig. 3C, bottom, and fig. S18B), although the belt-to-helix transition occurred at much higher (χ > ~5.0) particle densities—a threshold that is most likely governed by the size of the Ag domain.

We observed the emergence of helical nanoparticle superstructures during the self-assembly of superparamagnetic nanocrystals. We envision that the diversity of self-assembled superstructures could be further expanded by (i) decorating the surfaces of magnetite NCs with functional ligands (*32*), (ii) choosing SPM NCs of different shapes and compositions (e.g., Ni, Fe, and $CoFe_2O_4$) as starting materials, (iii) using mixtures of different NCs as building blocks (see fig. S19), and (iv) using complex or dynamic magnetic (*33*) fields during the self-assembly process.

REFERENCES AND NOTES

1. E. V. Shevchenko, D. V. Talapin, N. A. Kotov, S. O'Brien, C. B. Murray, *Nature* **439**, 55–59 (2006).
2. Z. Tang, Z. Zhang, Y. Wang, S. C. Glotzer, N. A. Kotov, *Science* **314**, 274–278 (2006).
3. A. M. Kalsin *et al.*, *Science* **312**, 420–424 (2006).
4. E. Auyeung *et al.*, *Nature* **505**, 73–77 (2014).
5. D. Nykypanchuk, M. M. Maye, D. van der Lelie, O. Gang, *Nature* **451**, 549–552 (2008).
6. T. Wang *et al.*, *Science* **338**, 358–363 (2012).
7. H. Cui *et al.*, *Science* **327**, 555–559 (2010).
8. M. A. Kostiainen *et al.*, *Nat. Nanotechnol.* **8**, 52–56 (2013).
9. K. Miszta *et al.*, *Nat. Mater.* **10**, 872–876 (2011).
10. K. J. M. Bishop, C. E. Wilmer, S. Soh, B. A. Grzybowski, *Small* **5**, 1600–1630 (2009).
11. E. V. Shevchenko, D. V. Talapin, S. O'Brien, C. B. Murray, *J. Am. Chem. Soc.* **127**, 8741–8747 (2005).
12. X. Ye, J. Chen, C. B. Murray, *J. Am. Chem. Soc.* **133**, 2613–2620 (2011).
13. D. Faivre, D. Schüler, *Chem. Rev.* **108**, 4875–4898 (2008).
14. R. E. Dunin-Borkowski *et al.*, *Science* **282**, 1868–1870 (1998).
15. M. W. Szyndler, R. M. Corn, *J. Phys. Chem. Lett.* **3**, 2320–2325 (2012).
16. M. V. Kovalenko *et al.*, *J. Am. Chem. Soc.* **129**, 6352–6353 (2007).
17. T. Wang *et al.*, *J. Am. Chem. Soc.* **134**, 18225–18228 (2012).
18. D. Kim *et al.*, *J. Am. Chem. Soc.* **131**, 454–455 (2009).
19. See supplementary materials on *Science* Online.
20. V. Aleksandrovic *et al.*, *ACS Nano* **2**, 1123–1130 (2008).
21. A. Dong, J. Chen, P. M. Vora, J. M. Kikkawa, C. B. Murray, *Nature* **466**, 474–477 (2010).
22. In that respect, our methodology is akin to assembling nanocrystals using the Langmuir-Blodgett technique. See also (*23*).
23. Large arrays of belts assembled from NCs of various compositions were previously prepared by evaporation-induced assembly (*24*); although this method bears some similarity to our results (e.g., NC assemblies were prepared at the liquid-air interface), the mechanism of assembly (based on contact-line instabilities) is conceptually different. In fact, we

did not observe the formation of any well-defined structures in the absence of an applied magnetic field (see, e.g., fig. S8J).
24. A. Dong *et al.*, *Nano Lett.* **11**, 841–846 (2011).
25. S. Brooks, A. Gelman, G. Jones, X.-L. Meng, *Handbook of Markov Chain Monte Carlo* (Chapman & Hall, London, 2011).
26. Z. Kakol, R. N. Pribble, J. M. Honig, *Solid State Commun.* **69**, 793–796 (1989).
27. Ü. Özgür, Y. Alivov, H. Morkoç, *J. Mater. Sci. Mater. Electron.* **20**, 789–834 (2009).
28. The formation of helices, and the self-assembly of NCs in our system in general, is likely facilitated by entropic forces; OA used in large excess during self-assembly may act as a depletion agent, inducing crystallization of NCs during hexane evaporation as reported previously (*29*).
29. D. Baranov *et al.*, *Nano Lett.* **10**, 743–749 (2010).
30. On the basis of measurements of electrophoretic mobility [see (*34*)] and the lack of literature reports on electric dipole moments of magnetite nanoparticles, we did not consider electrostatic and electric dipole-dipole interactions in our analysis of interparticle interactions. At the same time, we cannot exclude the possible presence of these interactions in our system.
31. S. Srivastava *et al.*, *Science* **327**, 1355–1359 (2010).
32. S. Das *et al.*, *Adv. Mater.* **25**, 422–426 (2013).
33. J. V. I. Timonen, M. Latikka, L. Leibler, R. H. A. Ras, O. Ikkala, *Science* **341**, 253–257 (2013).
34. Previous self-assembly experiments performed in nonpolar solvents excluded a significant role played by electrostatic interactions [e.g., (*35*, *36*)]. Although the degree of dissociation of OA in hexane (dielectric constant = 1.84) is negligible, the large excess of OA as well as the nature of our experimental setup (self-assembly at the liquid-air interface) might potentially promote dissociation of OA; to verify this possibility, we used a Malvern Zetasizer Nano ZS to perform electrophoretic mobility (μ_e) measurements of our nanocubes in hexane both in the absence and in the presence of additional OA (5% v/v). The results [0.00706 (±0.00104) × 10^{-4} cm^2 V^{-1} s^{-1} and 0.0218 (±0.00710) × 10^{-4} cm^2 V^{-1} s^{-1}, respectively] indicate that in both cases, the nanocubes are essentially neutral [compare with (*37*)].
35. Z. Chen, J. Moore, G. Radtke, H. Sirringhaus, S. O'Brien, *J. Am. Chem. Soc.* **129**, 15702–15709 (2007).
36. X. Ye *et al.*, *Nat. Chem.* **5**, 466–473 (2013).
37. S. A. Hasan, D. W. Kavich, J. H. Dickerson, *Chem. Commun.* **2009**, 3723–3725 (2009).

ACKNOWLEDGMENTS

Supported by Israel Science Foundation grant 1463/11, the G. M. J. Schmidt-Minerva Center for Supramolecular Architectures, and the Minerva Foundation with funding from the Federal German Ministry for Education and Research (R.K.) and by NSF Division of Materials Research grant 1309765 and American Chemical Society Petroleum Research Fund grant 53062-ND6 (P.K.).

SUPPLEMENTARY MATERIALS

www.sciencemag.org/content/345/6201/1149/suppl/DC1
Materials and Methods
Figs. S1 to S28
References (*38*–*92*)

31 March 2014; accepted 14 July 2014
Published online 24 July 2014;
10.1126/science.1254132

METAL ALLOYS

A fracture-resistant high-entropy alloy for cryogenic applications

Bernd Gludovatz,[1] Anton Hohenwarter,[2] Dhiraj Catoor,[3] Edwin H. Chang,[1] Easo P. George,[3,4]* Robert O. Ritchie[1,5]*

High-entropy alloys are equiatomic, multi-element systems that can crystallize as a single phase, despite containing multiple elements with different crystal structures. A rationale for this is that the configurational entropy contribution to the total free energy in alloys with five or more major elements may stabilize the solid-solution state relative to multiphase microstructures. We examined a five-element high-entropy alloy, CrMnFeCoNi, which forms a single-phase face-centered cubic solid solution, and found it to have exceptional damage tolerance with tensile strengths above 1 GPa and fracture toughness values exceeding 200 MPa·$m^{1/2}$. Furthermore, its mechanical properties actually improve at cryogenic temperatures; we attribute this to a transition from planar-slip dislocation activity at room temperature to deformation by mechanical nanotwinning with decreasing temperature, which results in continuous steady strain hardening.

Pure metals rarely display the mechanical properties required for structural applications. Consequently, alloying elements are added to achieve a desired microstructure or combination of mechanical properties, such as strength and toughness, although the resulting alloys invariably still involve a single dominant constituent, such as iron in steels or nickel in superalloys. Additionally, many such alloys, such as precipitation-hardened aluminum alloys, rely on the presence of a second phase for mechanical performance. High-entropy alloys (*1*–*3*) represent a radical departure from these notions. As equiatomic, multi-element metallic systems, they contain high concentrations (20 to 25 atomic percent) of multiple elements with different crystal structures but can crystallize as a single phase (*4*–*7*). In many respects, these alloys represent a new field of metallurgy that focuses attention away from the corners of alloy phase diagrams toward their centers; we believe that as this evolving field matures, a number of fascinating new materials may emerge.

The CrMnFeCoNi alloy under study here is a case in point. Although first identified a decade ago (*1*), the alloy had never been investigated mechanically until recently (*5*, *6*, *8*), yet is clearly scientifically interesting from several perspectives. It is not obvious why an equiatomic five-element alloy—where two of the elements (Cr and Fe) crystallize with the body-centered cubic (bcc) structure, one (Ni) as face-centered cubic (fcc), one (Co) as hexagonal close-packed (hcp), and one (Mn) with the complex *A*12 structure—should form a single-phase fcc structure. Furthermore, several of its properties are quite unlike those of pure fcc metals. Recent studies indicate that the alloy exhibits a strong temperature dependence of the yield strength between ambient and cryogenic temperatures, reminiscent of bcc metals and certain fcc solid-solution alloys (*6*). Strangely, any temperature-dependent effect of strain rate on strength appears to be marginal (*6*). Moreover, the marked temperature-dependent increase in strength is accompanied by a substantial increase in tensile ductility with decreasing temperature between 293 K and 77 K (*6*), which runs counter to most other materials where an inverse dependence of ductility and strength is invariably seen (*9*). Preliminary indications suggest that this may be principally a result of the alloy's high work-hardening capability, possibly associated with deformation-induced nanotwinning, which acts to delay the onset of any necking instability (i.e., localized plastic deformation that can lead to premature failure) to higher strains (*5*).

We prepared the CrMnFeCoNi alloy with high-purity elemental starting materials by arc melting and drop casting into rectangular-cross-section copper molds, followed by cold forging and cross rolling at room temperature into sheets roughly 10 mm thick. After recrystallization, the alloy had an equiaxed grain structure. Uniaxial tensile specimens and compact-tension fracture toughness specimens in general accordance with ASTM standard E1820 (*10*) were machined from these sheets by electrical discharge machining. [See (*11*) for details of the processing procedures, sample sizes, and testing methods.]

Figure 1A shows a backscattered electron (BSE) micrograph of the fully recrystallized microstructure with ~6-μm grains containing numerous recrystallization twins. Energy-dispersive x-ray (EDX) spectroscopy and x-ray diffraction (XRD) indicate the equiatomic elemental distribution and single-phase character of the alloy, respectively. Measured uniaxial stress-strain curves at room temperature (293 K), in a dry ice–alcohol mixture (200 K), and in liquid nitrogen (77 K) are plotted in Fig. 1B. With a decrease in temperature from 293 K to 77 K, the yield strength σ_y and ultimate tensile strength σ_{uts}

[1]Materials Sciences Division, Lawrence Berkeley National Laboratory, Berkeley, CA 94720, USA. [2]Department of Materials Physics, Montanuniversität Leoben and Erich Schmid Institute of Materials Science, Austrian Academy of Sciences, Leoben 8700, Austria. [3]Materials Sciences and Technology Division, Oak Ridge National Laboratory, Oak Ridge, TN 37831, USA. [4]Materials Sciences and Engineering Department, University of Tennessee, Knoxville, TN 37996, USA. [5]Department of Materials Science and Engineering, University of California, Berkeley, CA 94720, USA.
***Corresponding author. E-mail: georgeep@ornl.gov (E.P.G.); roritchie@lbl.gov (R.O.R.)**